



Noble-metal-free NiCu/CeO₂ catalysts for H₂ generation from hydrous hydrazine



Wooram Kang, Heng Guo¹, Arvind Varma*

Davidson School of Chemical Engineering, Purdue University, West Lafayette, IN 47907, United States

ARTICLE INFO

Keywords:

Noble-metal-free
NiCu/CeO₂
Hydrogen generation
Hydrous hydrazine
Solution combustion synthesis

ABSTRACT

The development of cost effective catalysts with high activity and 100% selectivity for hydrogen generation from the decomposition of hydrous hydrazine, a promising liquid-phase hydrogen carrier, is a critical challenge for the practical application of hydrous hydrazine to fuel cell vehicles. In this study, noble-metal-free NiCu/CeO₂ bimetallic catalysts were readily synthesized using one-step solution combustion synthesis (SCS). The addition of Cu to Ni/CeO₂ exhibited a synergistic effect to enhance the catalytic activity for the reaction. Catalyst characterization revealed that the improvement of catalytic performance is attributed to a combination of NiCu alloying, particle size of the active component, and formation of oxygen vacancy in the CeO₂ lattice. The tailored 13 wt% Ni_{0.5}Cu_{0.5}/CeO₂ catalyst exhibited 100% H₂ selectivity in the temperature range 30–70 °C and 3.2-fold higher turnover frequency (TOF) of 1450.0 h⁻¹ at 50 °C as compared to that of the Ni/CeO₂. This reactivity is also superior to that of most reported non-noble metal catalysts and is even comparable to noble metal-based catalysts.

1. Introduction

Hydrogen (H₂) is a promising energy carrier in many fields, especially transportation applications, because it has high gravimetric energy density (120 MJ/kg) as compared to conventional hydrocarbon fuels such as gasoline (44 MJ/kg) and diesel (42 MJ/kg), and environmental benign nature. In this regard, hydrogen fuel cell car using pure hydrogen gas fuel has been actively investigated. There are, however, still many technological barriers related to efficient production and on-board storage of hydrogen gas [1,2]. Liquid-phase hydrogen carriers have received much attention as a feasible alternative owing to their convenient transportation, handling, refueling, and potential availability of existing infrastructures for conventional liquid fuels [3,4]. Among liquid-phase hydrogen carriers, hydrous hydrazine (N₂H₄·H₂O) has been shown to be promising owing to its high hydrogen content (8.0 wt%), low material cost and capability of generating hydrogen at moderate temperature range (20–80 °C) which corresponds to the operating temperature of PEM fuel cell that is generally used for hydrogen fuel cell vehicles [5,6]. In addition, when hydrogen is generated from the complete decomposition of hydrazine [N₂H₄ (l) → N₂ (g) + 2H₂ (g)], the only byproduct is nitrogen, obviating the need for on-board collection system for spent fuel regeneration. However, incomplete decomposition [3N₂H₄ (l) → 4NH₃ (g) + N₂ (g)] can also occur due to

easier cleavage of N–N bond as compared to that of N–H, generating ammonia which is poison for PEM fuel cells [7–9]. Therefore, to maximize the efficiency of hydrous hydrazine as an on-board hydrogen carrier for fuel cell vehicles, the complete decomposition should be facilitated, while the incomplete decomposition should be avoided.

Towards this aim, various metal nanoparticles containing noble (Rh, Ir, Pt and Pd) and non-noble metals (Ni, Fe, Co and Cu) have been investigated to develop efficient catalysts for selective decomposition of hydrous hydrazine [10–13]. Among these, bimetallic catalysts containing Ni and noble metals, such as Pt, Rh and Ir, were shown to be effective for the reaction [14–16]. Nevertheless, the high cost of noble metals hinders their widespread application, so there has been significant effort devoted to the development of efficient noble metal-free catalysts [17–23]. A few studies have developed highly selective non-noble metal catalysts such as NiFe, FeNi/Cu, and Ni_{0.6}Fe_{0.4}Mo nanoparticles [17–19], while their catalytic activity is much lower than that of noble metal catalysts. Meanwhile, it has been reported that the use of metal oxides (Al₂O₃, CeO₂, La₂O₃ and MnO₂) as supports effectively promotes catalytic activity and selectivity [20,24–26]. For example, Al₂O₃ supported Ni catalyst exhibited 93% selectivity owing to the presence of strong basic sites provided by Al₂O₃, while CeO₂ supported Ni catalyst showed 99% selectivity owing to the modified electronic property of Ni with CeO₂ nearby through strong metal-support

* Corresponding author.

E-mail address: avarma@purdue.edu (A. Varma).

¹ Present address: School of Material Science and Engineering, Tsinghua University, Beijing, 100084, China.

interaction [20,24]. However, these supported catalysts require complicated preparation processes such as multistep synthesis and long reaction time. Thus, exploring a facile method to obtain non-noble metal catalysts with excellent catalytic activity and 100% selectivity for hydrogen generation from hydrous hydrazine is of great interest and a challenge.

In this study, a simple one-step solution combustion synthesis (SCS) was used to prepare noble-metal-free catalysts for hydrogen generation from hydrous hydrazine. SCS is a self-sustained process where the main source of energy is the combustion reaction between a metal oxidizer and a fuel, allowing to simply and rapidly synthesize a variety of metal and metal oxide nanopowders with uniform composition and porous structure [27]. Our prior work demonstrated that, owing to its highly porous structure and the enhanced strong metal-support interaction (e.g., formation of oxygen vacancy in CeO_2 lattice), Ni/CeO_2 catalysts prepared by SCS with optimized synthesis conditions exhibited 100% selectivity for hydrogen generation from hydrous hydrazine and the highest catalytic activity among all prior reported catalysts containing Ni alone [28]. In the present work, to develop cost-effective and more efficient catalysts, CeO_2 supported Ni-Cu bimetallic catalysts were synthesized using SCS. Although Cu has been widely used together with Ni to obtain synergistic effect for several important reactions such as water-gas shift and reforming [29,30], the exploration of this CeO_2 supported bimetallic catalyst has not been reported for hydrogen generation from hydrous hydrazine. Remarkably, our study found for the first time that the concomitant use of Cu with Ni/CeO_2 promotes the catalytic activity significantly. Among the investigated samples, 13 wt% $\text{Ni}_{0.5}\text{Cu}_{0.5}/\text{CeO}_2$ catalysts exhibited superior activity with turnover frequency (TOF) of 1450.0 h^{-1} at 50°C , which is 3.2 times higher than that of Ni/CeO_2 , and selectivity for hydrogen generation was 100% in the temperature range 30 to 70°C . Characterization revealed the reason for the synergistic effect observed for the NiCu/CeO_2 catalysts.

2. Experimental

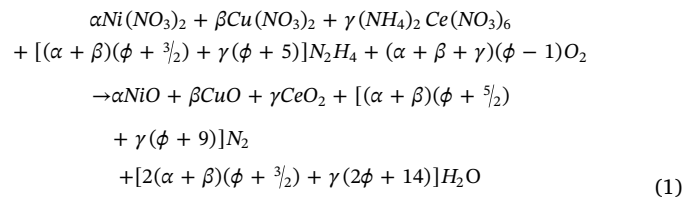
2.1. Materials

Nickel nitrate hexahydrate [$\text{Ni}(\text{NO}_3)_2 \cdot 6\text{H}_2\text{O}$, 98%], cerium ammonium nitrate [$(\text{NH}_4)_2\text{Ce}(\text{NO}_3)_6$, 98 + %], copper nitrate trihydrate [$\text{Cu}(\text{NO}_3)_2 \cdot 3\text{H}_2\text{O}$, 98 + %], and hydrous hydrazine ($\text{N}_2\text{H}_4 \cdot \text{H}_2\text{O}$, 99 + %) were purchased from Alfa Aesar. Sodium hydroxide (NaOH , 50% in H_2O) and tetraethyl orthosilicate [$\text{Si}(\text{OC}_2\text{H}_5)_4$] were obtained from Sigma-Aldrich. The chemicals were used without further purification. Deionized water was used throughout.

2.2. Catalyst preparation

NiCu/CeO_2 catalysts were synthesized by solution combustion synthesis (SCS). Typically, to prepare $\text{Ni}_{1-x}\text{Cu}_x/\text{CeO}_2$ catalysts with different Ni:Cu molar ratios ($x = 0, 0.25, 0.5, 0.75$, and 1), a stoichiometric amount of metal oxidizers [$\text{Ni}(\text{NO}_3)_2 \cdot 6\text{H}_2\text{O}$, $\text{Cu}(\text{NO}_3)_2 \cdot 3\text{H}_2\text{O}$, and $(\text{NH}_4)_2\text{Ce}(\text{NO}_3)_6$] were dissolved in a minimum amount of deionized water in a glass beaker and then $\text{N}_2\text{H}_4 \cdot \text{H}_2\text{O}$ as a fuel, was added into the solution. After thorough stirring, the mixture was placed in a preheated furnace to induce self-sustained combustion. After some time, the solution began to boil and then ignition occurred, followed by rapid increase of temperature and evolution of a large quantity of gases. The temperature change during the combustion process was monitored using a sensitive K-type thermocouple with a tip diameter of 0.125 mm to determine the maximum combustion temperature. The experimental error for the measurement of maximum combustion temperature was determined to be less than $\pm 10\%$. After combustion, the obtained metal oxide powders were removed from the furnace, calcined at 400°C for 4 h in air, and then treated at 400°C for 1 h in a flow of 10 vol% hydrogen (balance nitrogen) to reduce NiO and CuO to Ni and Cu, respectively. For comparison, $\text{Ni}_{0.5}\text{Cu}_{0.5}/\text{SiO}_2$

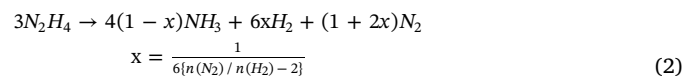
samples were also prepared using SCS, followed by calcination and reduction process similar to that for $\text{Ni}_{1-x}\text{Cu}_x/\text{CeO}_2$ catalysts. Since the nitrate precursor of silicon as an oxidizer for SCS is not available commercially, $\text{SiO}(\text{NO}_3)_2$ was first synthesized from the reaction of tetraethyl orthosilicate with nitric acid and then was used for SCS. The stoichiometric combustion reaction of the system for preparing $\text{Ni}_{1-x}\text{Cu}_x/\text{CeO}_2$ catalysts is shown in the equation below.



In the above equation, ϕ is defined as the fuel-to-oxidizer ratio and α , β , and γ are the number of moles of Ni, Cu, and Ce precursors, respectively. Besides, on the basis of the above equation, the number of moles of evolved gases per mole of product for each case was calculated to estimate the level of gas evolution. For all the catalysts studied in this work, the total loading of metals and ϕ were maintained at 13 wt% and 2, respectively.

2.3. H_2 generation from hydrous hydrazine decomposition

The catalytic decomposition reaction of $\text{N}_2\text{H}_4 \cdot \text{H}_2\text{O}$ was performed at the temperature range of 30–80 °C in a stainless-steel reactor (Parr Instrument Company, Model 4592) with external heating jacket. Aqueous reactant solution containing $\text{N}_2\text{H}_4 \cdot \text{H}_2\text{O}$ (0.4 M) and NaOH (6 M) was prepared by adding 0.2 ml of $\text{N}_2\text{H}_4 \cdot \text{H}_2\text{O}$ to 10 ml of NaOH solution (6.1 M) under magnetic stirring. The reaction was initiated by injecting 2 ml of the prepared solution into the reactor where the catalyst was placed under stirring of 1100 rpm and argon (99.999%) atmosphere. In all cases, the molar ratio of metal in the catalyst to hydrous hydrazine was kept fixed at 1:5. The reaction progress was monitored by measuring reactor pressure using a transducer (Omega Engineering PX35D1). After reaction completion, the composition of product gas was analyzed by mass spectrometer (Hiden Analytical HPR-20) to obtain the molar ratio of N_2 to H_2 and to assess the presence of NH_3 . The selectivity for H_2 generation (x) was calculated based on the overall reaction, as follows:



where $n(\text{N}_2)$ and $n(\text{H}_2)$ are the moles of produced N_2 and H_2 , respectively. The TOF was calculated, as follows:

$$\text{TOF (h}^{-1}\text{)} = \frac{n(\text{H}_2)}{n(\text{Ni}) \times d \times t} \quad (3)$$

where $n(\text{Ni})$ is the moles of Ni in the catalyst, t is the reaction time for 50% conversion of hydrous hydrazine and d is the metal dispersion of Ni or NiCu alloy. The value of d was calculated from mean metal particle size, Ni or NiCu, determined by XRD [31]. The reported TOF values are averages from 2 to 5 experiments. For testing the durability of catalysts, the catalytic reaction was repeated 6 times by adding another equivalent of $\text{N}_2\text{H}_4 \cdot \text{H}_2\text{O}$ into the reactor after completion of the previous run.

2.4. Catalyst characterization

Powder X-ray diffraction (XRD) patterns of the samples were obtained using a Rigaku SmartLab X-ray Diffractometer with $\text{Cu K}\alpha$ radiation ($\lambda = 0.1541 \text{ nm}$) and scanning range (2θ) of 20–80°, operated at $40 \text{ kV} \times 40 \text{ mA}$. The mean particle size of components in catalysts was determined from the XRD patterns by the Scherrer equation. N_2

adsorption-desorption isotherms of the samples were measured at -196°C using a Quantachrome Autosorb. On the basis of the isotherm data, the specific surface area and total pore volume were obtained using the multi-point Brunauer-Emmett-Teller (BET) and Barrett-Joyner-Halenda (BJH) methods, respectively. Scanning electron microscopy (SEM) images were obtained at 5 kV acceleration voltage using an FEI Nova NanoSEM. Semi-quantitative elemental analysis was conducted at 10 kV acceleration voltage using a JCM-6000PLUS NeoScope Benchtop SEM equipped with an energy dispersive spectroscopy (EDS). Raman spectra were acquired using a Thermo Scientific DXR2 spectrometer with a $50\times$ objective, 633 nm filter, spectral resolution of $\sim 3\text{ cm}^{-1}$, and a power of 5 mW. X-ray photoelectron spectroscopy (XPS) studies were carried out using a Kratos Axis Ultra DLD system with monochromatic AlKa (1486.6 eV) X-ray source to examine chemical and electronic states of the elements on the catalyst surface. The binding energy of C1s (284.4 eV) was used as an internal standard. The Ni and Cu contents in the catalysts were measured using an atomic absorption spectroscopy (AAS) on a PerkinElmer AAnalyst 300. The H_2 temperature programmed reduction (H_2 -TPR) experiments were performed using a Gow-Mac Model 20 thermal conductivity detector. In a typical test, 200 mg of catalyst was loaded in the middle of a quartz tube reactor, with quartz wool supports on both sides. Before the reduction, the catalyst was cleaned by purging N_2 gas for 1 h at 200°C and then cooled down to room temperature. The reduction was performed under a 10 vol% H_2 (balance N_2) gas flow with a heating rate of $10^{\circ}\text{C}/\text{min}$ from room temperature to 650°C .

3. Results and discussion

3.1. Catalytic performance of NiCu/CeO_2 catalysts

The series of $\text{Ni}_{1-x}\text{Cu}_x/\text{CeO}_2$ ($x = 0, 0.25, 0.5, 0.75$, and 1) catalysts were prepared by SCS. The loading amount of metals (Ni + Cu) was fixed at 13 wt% for all samples, while the actual metal contents were determined by atomic absorption spectroscopy (Table S1). The catalytic decomposition of hydrous hydrazine was performed in the presence of NaOH (6 M) at 50°C under magnetic stirring of 1100 rpm [$n(\text{metal})/n(\text{N}_2\text{H}_4) = 0.2$].

The time course plots of the decomposition of hydrous hydrazine at 50°C over the $\text{Ni}_{1-x}\text{Cu}_x/\text{CeO}_2$ ($x = 0, 0.25, 0.5, 0.75$, and 1) catalysts are shown in Fig. 1. It can be observed that the catalytic performance strongly depends on the metal composition. For the Ni/CeO_2 monometallic catalyst, gas evolution from the decomposition of hydrous hydrazine is complete within 24 min and the molar ratio of product gas

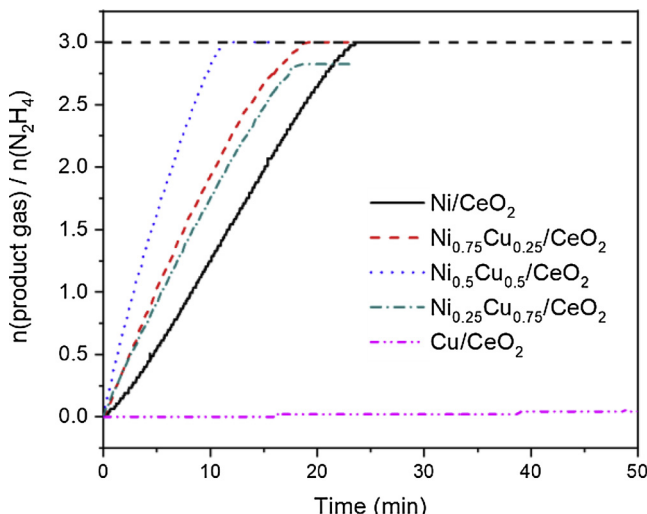


Fig. 1. Time course plots of the decomposition of hydrous hydrazine at 50°C over $\text{Ni}_{1-x}\text{Cu}_x/\text{CeO}_2$ ($x = 0, 0.25, 0.5, 0.75$, and 1) catalysts.

to N_2H_4 [$n(\text{product gas})/n(\text{N}_2\text{H}_4)$] reaches 3 which implies only at 100% conversion and 100% H_2 selectivity. The H_2 selectivity was further confirmed by mass spectroscopy, revealing that the product gas contains only H_2 and N_2 in the molar ratio $\text{H}_2/\text{N}_2 = 2.0$.

The addition of Cu to Ni/CeO_2 appears to create a synergistic effect that promotes catalytic activity for the reaction. As the Cu content increases further ($x = 0\text{--}0.5$), the reaction rate increases gradually while the H_2 selectivity remains at 100%. Increasing the amount of Cu ($x = 0.5\text{--}1$) leads to a decrease in both catalytic activity and H_2 selectivity. Notably, the Cu/CeO_2 ($x = 1$) catalyst is totally inactive, implying that Ni is the key active component for the reaction. This is consistent with previous studies that Ni is the representative active non-noble metal and Cu itself is inert for hydrous hydrazine decomposition [5].

Consequently, the optimal catalytic performance was found for $\text{Ni}_{0.5}\text{Cu}_{0.5}/\text{CeO}_2$ catalysts, exhibiting 100% H_2 selectivity with a TOF of 1450.0 h^{-1} at 50°C which is about 3.2-fold higher than the monometallic Ni/CeO_2 catalyst (447.2 h^{-1}). This catalytic activity is superior to that of most reported non-noble metal catalysts and is even comparable to that of many catalysts containing noble-metals such as Pt, Ir and Pd (Table S2) [17,18,23,32–34]. Moreover, the facile one-step SCS method to prepare the catalysts provides some advantages over alternative methods used in the literature which require surfactants and/or time-consuming processes (e.g. aging and drying) [21,35].

Note that the reaction was performed under conditions where the reaction is not controlled by mass transfer. The reaction rate at the highest reaction temperature (80°C), where external mass transfer limitation would be the most severe, was independent of the agitation speed range 300–1100 rpm (Fig. S1) and the average powder size of the $\text{Ni}_{0.5}\text{Cu}_{0.5}/\text{CeO}_2$ catalysts was $13.2\text{ }\mu\text{m}$ (Fig. S2). Accordingly, the external and internal mass transfer limitations can be assumed to be negligible. Therefore, the synergistic effect observed for the NiCu/CeO_2 catalysts originates essentially from the intrinsic performance. More specifically, the enhanced activity of the NiCu/CeO_2 samples may be attributed to a combination of the modified electronic structure of catalyst surface, the small particle size of active component, and the increased amount of oxygen vacancy within CeO_2 structure, as discussed later.

Fig. 2 shows that the time course plots for the decomposition of hydrous hydrazine over $\text{Ni}_{0.5}\text{Cu}_{0.5}/\text{CeO}_2$ catalyst at different temperatures. The standard deviation of the reaction time for 50% conversion is indicated by the error bars. The reaction rate significantly increased about 45-fold with increase in the reaction temperature from 30 to 80°C . The TOFs for 50% conversion were $180.4, 516.6, 1450.0, 2480.5, 4817.0$, and 8225.7 h^{-1} at 30, 40, 50, 60, 70, and 80°C , respectively.

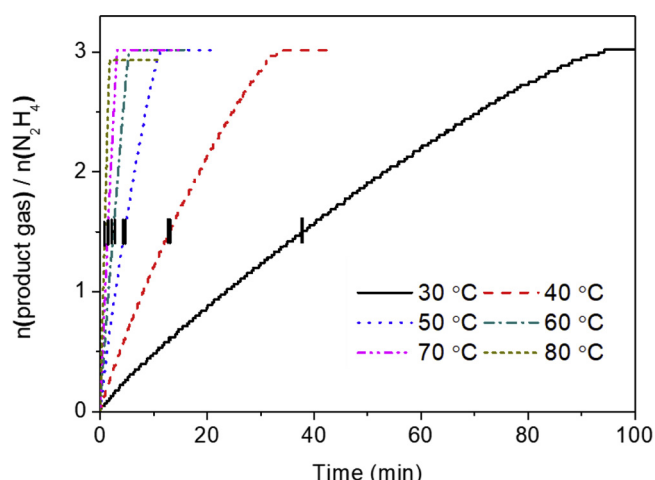


Fig. 2. Time course plots of the decomposition of hydrous hydrazine over $\text{Ni}_{0.5}\text{Cu}_{0.5}/\text{CeO}_2$ catalyst as a function of temperature.

The H₂ selectivity remained 100% in the temperature range 30–70 °C. When the temperature increased further to 80 °C, the selectivity decreased to 97% owing to thermodynamic reasons as reported elsewhere [20]. The apparent activation energy (E_a) values for catalytic decomposition of hydrous hydrazine over Ni/CeO₂, Ni_{0.75}Cu_{0.25}/CeO₂, Ni_{0.5}Cu_{0.5}/CeO₂, and Ni_{0.25}Cu_{0.75}/CeO₂ catalyst were determined to be 67.3, 64.2, 63.0, and 64.8 kJ/mol, respectively (Fig. S3). The Ni/CeO₂ monometallic catalyst exhibits somewhat higher activation energy than the NiCu/CeO₂ catalysts, which indicates a synergistic effect in the decomposition of hydrous hydrazine over NiCu/CeO₂ bimetallic catalysts.

Further reaction experiments were conducted for the most active catalyst (Ni_{0.5}Cu_{0.5}/CeO₂). In durability test, the Ni_{0.5}Cu_{0.5}/CeO₂ catalyst retained 100% H₂ selectivity over 6 runs and exhibited only a small decrease in activity (Fig. S4). There was not an obvious change of metal phases for the used catalysts according to the X-ray diffraction (XRD) patterns (Fig. S5). The slight deactivation may be attributed to a decrease in the active Ni sites by the strong binding of N₂ species on the catalyst surface [36].

3.2. Characterization of NiCu/CeO₂ catalysts

In this section, the NiCu/CeO₂ catalysts were characterized by BET, SEM-EDS, XRD, XPS, Raman, and H₂-TPR techniques to identifying the reasons for the promoting effect of Cu on the catalytic performance. These characterizations are described separately below.

3.2.1. N₂ adsorption-desorption isotherm analysis

The textural properties of Ni_{1-x}Cu_x/CeO₂ (x = 0, 0.25, 0.5, 0.75, and 1) catalysts were confirmed by N₂ adsorption-desorption isotherm as shown in Fig. S6. All the samples showed similar isotherm shapes and exhibited the characteristic feature of a composite type II/IV isotherm with a type H3 hysteresis loop, which indicates disordered porous materials with a non-uniform pore network and a broad pore size distribution in the meso- and macro- ranges [37]. This disordered pore structure may be related to the nature of SCS where pore structure is formed by gases evolved during the combustion process. From the isotherms of the samples, BET specific surface area and total pore volume were obtained (Table 1). The samples have similar values of specific surface area (16.7–20.6 m²/g) and total pore volume (0.077–0.088 cm³/g). It suggests that the addition of Cu to Ni/CeO₂ does not affect strongly the textural properties of the catalysts.

As noted above, the textural properties of SCS-derived products depend strongly on gas evolution during combustion, which promotes porosity of products and inhibits particle agglomeration by dissipating the heat. The degree of gas evolution can be estimated indirectly from the amount of evolved gases. The number of moles of evolved gases per mole of product for each case was calculated based on the combustion reaction equation (in Supporting Information) and is shown in Table 1. As expected, the amounts of gases for each case are similar (21.6–21.9 mol). The Cu/CeO₂ shows relatively smaller specific surface area because of higher maximum combustion temperature which leads to particle agglomeration and shrinkage of pore structure.

Table 1

Textural properties and combustion characteristics of Ni_{1-x}Cu_x/CeO₂ (x = 0, 0.25, 0.5, 0.75, and 1) catalysts.

Sample	Particle size (nm)		CeO ₂ lattice parameter (Å)	BET surface area (m ² /g)	Pore volume (cm ³ /g)	Maximum temperature (°C)	Amount of gases (mol)
	Ni or alloy	CeO ₂					
Ni/CeO ₂	21.7	27.7	5.4094	16.7	0.077	820	21.6
Ni _{0.75} Cu _{0.25} /CeO ₂	18.1	22.4	5.4161	18.8	0.088	783	21.7
Ni _{0.5} Cu _{0.5} /CeO ₂	13.1	18.1	5.4210	19.2	0.083	708	21.6
Ni _{0.25} Cu _{0.75} /CeO ₂	18.3	20.5	5.4179	20.6	0.083	798	21.9
Cu/CeO ₂	–	47.1	5.4099	12.3	0.050	900	21.9

3.2.2. Scanning electron micrographs and energy-dispersive X-ray spectroscopy (SEM-EDS)

The morphologies of the Ni_{0.5}Cu_{0.5}/CeO₂ catalyst were analyzed by scanning electron microscopy (SEM) analysis and the images are presented in Fig. 3. Fig. 3a and b show that the material has a sponge-like porous structure with a broad pore size distribution, revealing the presence of large macro-pores, and small macro-pores and meso-pores, respectively. These roundish pores are formed by the rapid gas evolution during combustion. This porous structure with a broad pore size distribution is consistent with the results of N₂ adsorption-desorption analysis. The elemental mapping analysis by energy dispersive spectroscopy (EDS) demonstrates the uniform dispersion of Cu and Ni elements over CeO₂ support (Fig. 3c and d). From the SEM-EDS result, the molar ratio of Ni to Cu was determined to be 0.53:0.47 which agrees well with the AAS result (0.52:0.48).

3.2.3. X-ray diffraction (XRD) studies

Fig. 4a shows the XRD patterns of the Ni_{1-x}Cu_x/CeO₂ catalysts. All samples clearly exhibit the diffraction pattern of the cubic fluorite-type CeO₂ (PDF No. 01-073-6328). The pattern of Ni/CeO₂ shows a peak at 2θ = 44.5°, corresponding to Ni(111) phase (PDF No. 01-070-0989) while Cu/CeO₂ exhibits a peak at 2θ = 43.3°, corresponding to Cu(111) phase (PDF No. 01-089-2838). For the NiCu/CeO₂ catalysts, the (111) peak of active component Ni shifts towards the peak of Cu(111) in Cu/CeO₂ as the Cu content increases (Fig. 4b). It may be attributed to the expansion of the Ni lattice due to the partial incorporation of larger Cu (lattice parameter = 0.362 nm) into the lattice of Ni (0.352 nm), indicating the formation of NiCu alloy phase. Meanwhile, Fig. 4b reveals that the peak position of Cu phase is not changed by the metal composition. This clearly indicates that the NiCu/CeO₂ catalysts have a composite structure consisting of NiCu alloy and Cu phases.

The NiCu alloying may be one of the possible reasons for the variation of catalytic performance and activation energy with metal composition. For NiCu bimetallic systems, it was shown theoretically and experimentally that the interaction between reactant and metal surface depends on the electronic structure of the alloy surface which can be altered by metal composition [38–40]. The interaction strength between NiCu alloy surface and reacting species would lie in between Ni and Cu monometallic systems, which possess too strong or too weak interaction. Therefore, according to the Sabatier principle, NiCu alloying explains the improved activity of NiCu/CeO₂ catalysts. In addition, Yen et al. reported that NiCu nanoparticles supported on mesoporous carbon nanosphere (MCNS) with different metal composition exhibit improved catalytic performance for hydrous hydrazine decomposition as compared to monometallic catalysts owing to modification of the surface electronic structure by the NiCu alloying and the highest catalytic activity was found for Ni_{0.5}Cu_{0.5}/MCNS [32].

Fig. S7 shows the lattice parameter of NiCu alloy for the samples calculated from the XRD results. The lattice parameter gradually increases with bulk Cu content. To evaluate the degree of alloying of Ni with Cu, the theoretical lattice parameter was calculated using Vegard's law, where homogeneous alloying is assumed [41]. With increasing Cu content, the degree of alloying increases from 36% (Ni_{0.75}Cu_{0.25}/CeO₂) to 48% (Ni_{0.5}Cu_{0.5}/CeO₂). When the Cu content increases further,

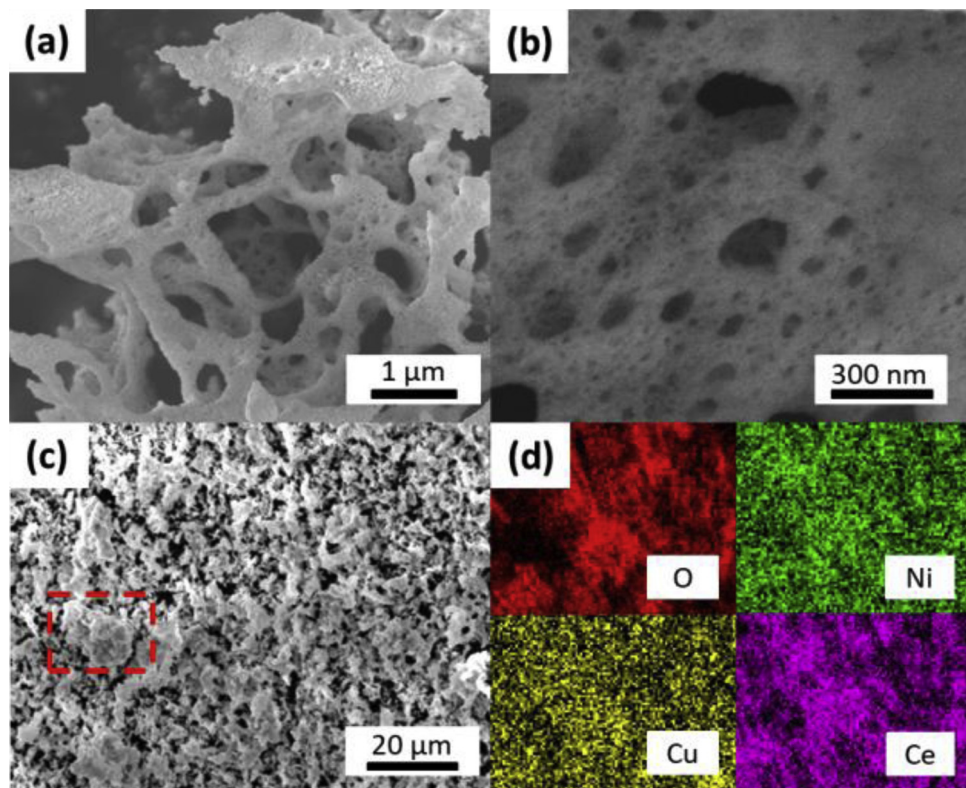


Fig. 3. (a,b,c) SEM images and (d) energy dispersive spectroscopy (EDS) elemental mapping of $\text{Ni}_{0.5}\text{Cu}_{0.5}/\text{CeO}_2$ catalyst.

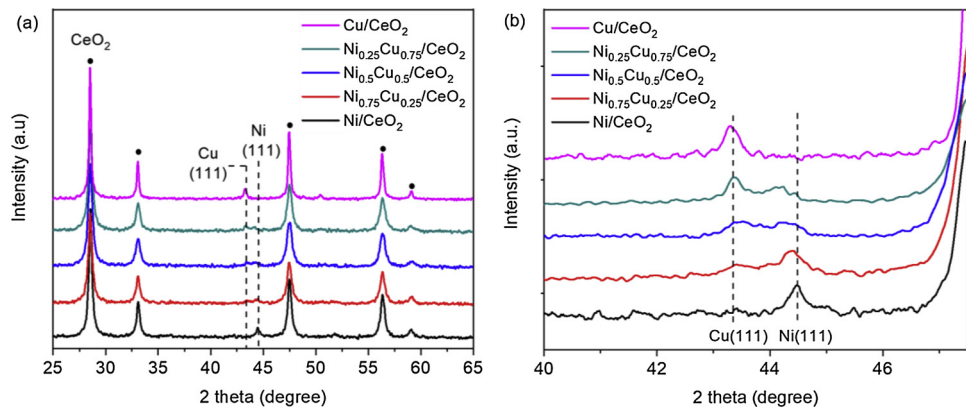


Fig. 4. (a) XRD patterns of $\text{Ni}_{1-x}\text{Cu}_x/\text{CeO}_2$ ($x = 0, 0.25, 0.5, 0.75$, and 1) catalysts and (b) detail of the range $2\theta = 40\text{--}47.5^\circ$.

however, the degree of alloying decreases slightly to 45% ($\text{Ni}_{0.25}\text{Cu}_{0.75}/\text{CeO}_2$). It appears that, at high Cu contents, the individual metal atoms prefer to segregate rather than to form a homogeneous alloy [42].

In addition to NiCu alloying, particle size of the active component is also a critical factor affecting the catalytic performance. For SCS, the particle size of products depends strongly on the combustion temperature which can be controlled by adjusting the type and ratio of precursors. In general, higher combustion temperature leads to larger particle size by particle growth and agglomeration. Table 1 shows the measured maximum temperature during combustion process and the average particle size of Ni or NiCu in the catalysts. The particle size was calculated based on the XRD data using the Scherrer equation [43]. As expected, the trend of the particle size agrees well with the maximum combustion temperature. Notably, the combustion temperature of NiCu/CeO₂ bimetallic systems is relatively lower than Ni/CeO₂ mono-metallic case, resulting in smaller metal particles. Owing to the lowest combustion temperature, the smallest NiCu alloy particle size (13.1 ± 0.4 nm) was obtained for $\text{Ni}_{0.5}\text{Cu}_{0.5}/\text{CeO}_2$. As shown in Fig. 1,

the activity of the catalysts appears to increase as the active metal particle size decreases since small metal particle size would provide more active sites for catalytic reactions. Therefore, this may be another reason why NiCu/CeO₂ bimetallic catalysts show better catalytic performance than Ni/CeO₂ and $\text{Ni}_{0.5}\text{Cu}_{0.5}/\text{CeO}_2$ exhibits the highest catalytic activity.

It is also known that interaction between metals and support has a significant impact on the catalyst performance. To investigate support effect, $\text{Ni}_{0.5}\text{Cu}_{0.5}/\text{SiO}_2$ catalyst with 13 wt% total metal loading was synthesized using SCS. The XRD pattern of $\text{Ni}_{0.5}\text{Cu}_{0.5}/\text{SiO}_2$ exhibits the characteristic peaks of amorphous SiO₂, NiCu alloy, and segregated Cu (Fig. S8a). Average particle size of NiCu alloy and degree of alloying are 15.1 nm and 45%, respectively (Fig. S8b). These values are close to those found for $\text{Ni}_{0.5}\text{Cu}_{0.5}/\text{CeO}_2$ (13.1 nm and 48%). Further, the $\text{Ni}_{0.5}\text{Cu}_{0.5}$ catalysts supported on different supports were tested in the decomposition of hydrous hydrazine. To avoid the dissolution of amorphous SiO₂ in NaOH solution during reaction, the experiments were carried out under water medium (0 M NaOH). Due to the absence

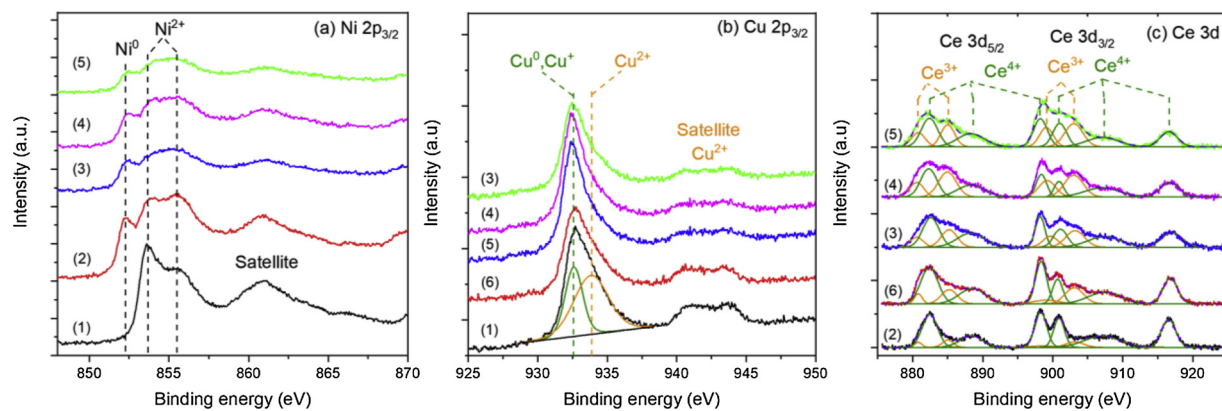


Fig. 5. (a) Ni 2p_{3/2}, (b) Cu 2p_{3/2}, and (c) Ce 3d XPS spectra of the samples: (1) NiO_{0.5}CuO_{0.5}/CeO₂; (2) Ni/CeO₂; (3) Ni_{0.75}Cu_{0.25}/CeO₂; (4) Ni_{0.5}Cu_{0.5}/CeO₂; (5) Ni_{0.25}Cu_{0.75}/CeO₂; (6) Cu/CeO₂.

of NaOH which promotes reaction rate and H₂ selectivity, the catalytic performance of Ni_{0.5}Cu_{0.5}/CeO₂ under water medium is worse than that under NaOH solution. Fig. S9 shows that Ni_{0.5}Cu_{0.5}/CeO₂ has much better catalytic activity (892.8 h⁻¹) and H₂ selectivity (75%) than Ni_{0.5}Cu_{0.5}/SiO₂ (33.7 h⁻¹, 50%). Interestingly, despite the fact that metal particle size and degree of alloying of both catalysts are similar, the difference in activity and H₂ selectivity is significant, which suggests that the catalyst support plays a critical role in the decomposition of hydrous hydrazine.

Lattice parameter of CeO₂ for the Ni_{1-x}Cu_x/CeO₂ catalysts ($x = 0, 0.25, 0.5, 0.75$, and 1) is shown in Table 1. Notably, it was found that the CeO₂ lattice constant of all the Ni_{1-x}Cu_x/CeO₂ catalysts is larger than that of pure CeO₂ (5.4082 Å). This lattice expansion may be related to the formation of Ni-O-Ce and/or Cu-O-Ce solid solutions by strong interaction between metals and CeO₂. It is known that metal cations such as Ni and Cu ions can incorporate into CeO₂ lattice forming Ni-O-Ce and Cu-O-Ce solid solutions. This process is accompanied by reduction of Ce⁴⁺ to Ce³⁺ as well as generation of oxygen vacancies in CeO₂ structure to compensate for the charge difference between metal cations and Ce⁴⁺ [44,45]. Since the ionic radius of Ce³⁺ (0.107 nm) is about 14% larger than that of Ce⁴⁺ (0.094 nm), the formation of the solid solutions results in lattice expansion [46]. It was also found that the lattice expansion of CeO₂ for the NiCu/CeO₂ bimetallic catalysts is more pronounced than that for monometallic catalysts. This suggests that the presence of Ni and Cu together may promote the formation of oxygen vacancy in CeO₂.

It is known that the oxygen vacancies in CeO₂ have a significant role to improve redox properties of Ce⁴⁺/Ce³⁺ and hence promote catalytic activity of CeO₂-based materials for many applications [47–49]. For hydrous hydrazine decomposition reaction over ceria supported catalysts, it was reported that the oxygen vacancy in CeO₂ structure modifies the electronic ability of nearby Ni atoms as an electron donor while Ce³⁺ acts as a Lewis base. Both oxygen vacancy and Ce³⁺ can enhance the adsorption of N₂H₄ molecules on Ni surface and N–H bond dissociation instead of N–N bond on Ni, resulting in high catalytic activity and H₂ selectivity [23,24]. The XRD results indicate that the Ni_{0.5}Cu_{0.5}/CeO₂ catalyst has the largest CeO₂ lattice parameter, possibly resulting from the presence of the largest amount of Ce³⁺ ions and oxygen vacancies in the CeO₂ lattice. Therefore, this feature is also related to better performance of the Ni_{0.5}Cu_{0.5}/CeO₂ catalyst towards hydrogen generation from hydrous hydrazine.

The enhanced formation of oxygen vacancy for the bimetallic cases may be ascribed to a synergistic interaction among Ni, Cu and CeO₂. It was reported that, for Cu-Ce catalyst system, Cu ions can exist as Cu⁺ as well as Cu²⁺ by a strong metal-support interaction (Ce⁴⁺ + Cu⁺ ↔ Ce³⁺ + Cu²⁺) and the addition of Ni significantly increases the concentration of Cu⁺ ion [50–52]. In addition, it is known that Cu⁺ can easily incorporate into CeO₂ lattice to form Cu-O-Ce solid solution

owing to the similarity of the ion radius of Cu⁺ (0.096 nm) and Ce⁴⁺ (Ce⁴⁺, 0.094 nm) [45,46]. Thus, the increased concentration of Cu⁺ may increase the number of Ce³⁺ ions and oxygen vacancies in CeO₂ structure. Moreover, the distorted CeO₂ structure by Cu⁺ ions may further facilitate the incorporation of smaller Ni²⁺ (0.072 nm) and Cu²⁺ (0.072 nm) cations into the CeO₂ lattice to form Ni-O-Ce and Cu-O-Ce solid solutions which essentially create oxygen vacancies.

On the other hand, it has also been known that decrease in the particle size of CeO₂ leads to an increase in the lattice strain, causing the formation of oxygen vacancies [53,54]. This effect may also contribute to increase the concentration of oxygen vacancy in the NiCu/CeO₂ catalysts which have smaller size of CeO₂ particles than Ni/CeO₂ and Cu/CeO₂ (Table 1). This may be attributed to the lower maximum combustion temperature. As observed for the particle size of Ni in the catalysts, the trend of the particle size of CeO₂ corresponds well to the maximum combustion temperature. The effect of the incorporation of metal cations into CeO₂, however, predominates over the effect of CeO₂ particle size. Although the CeO₂ size of the Cu/CeO₂ is larger than that of the Ni/CeO₂, the CeO₂ lattice parameter for the Cu/CeO₂ is larger than that of the Ni/CeO₂.

3.2.4. X-ray photoelectron spectroscopy (XPS) results

In order to investigate the chemical and electronic states of the elements on the catalyst surface, XPS analysis was carried out. Fig. 5a shows the Ni 2p_{3/2} XPS spectra of the samples NiO_{0.5}CuO_{0.5}/CeO₂, Ni/CeO₂, Ni_{0.75}Cu_{0.25}/CeO₂, Ni_{0.5}Cu_{0.5}/CeO₂, and Ni_{0.25}Cu_{0.75}/CeO₂. For the NiO_{0.5}CuO_{0.5}/CeO₂ oxide sample, a strong peak near 854.5 eV and a satellite feature in the range 858–865 eV are observed and are characteristic of Ni²⁺ [55]. The main peak is composed of two overlapped peaks at a low (853.6 eV) and a high (855.4 eV) binding energy. The peak at lower binding energy corresponds to Ni²⁺ ions in NiO particles while the peak at higher binding energy represents Ni²⁺ ions surrounded by Ce⁴⁺ ions in the form of Ni-O-Ce solid solution [55]. Thus, this indicates that NiO and Ni-O-Ce solid solution coexist on the surface of the oxide samples. For the Ni/CeO₂ sample, a peak associated with metallic Ni⁰ can be observed at 852.3 eV. In addition, in the oxide sample, the peak intensity of Ni²⁺ in NiO is stronger than that of Ni²⁺ in the solid solution, while the two peaks for Ni²⁺ in Ni/CeO₂ catalysts exhibit similar intensity. This indicates that metallic Ni is mainly formed from the reduction of NiO since the formed Ni-O-Ce solid solution is stable and difficult to reduce [56]. For the NiCu/CeO₂ bimetallic samples, it is seen that the binding energy of Ni⁰ changes by approximately 0.2 to 0.3 eV. The XPS peak shift of metallic species for alloys of transition metals has been commonly reported since the binding energy can be sensitively changed by formation of alloy structure [57,58]. The formation of NiCu alloy in the NiCu/CeO₂ catalysts was also confirmed from the XRD results. Therefore, the shift of Ni⁰ peak observed in the NiCu/CeO₂ samples may be attributed to NiCu

alloying. The XPS spectra of the samples after reduction still exhibit a significant amount of Ni^{2+} ions possibly due to the presence of high concentration of Ni-O-Ce solid solution and the aerobic oxidation of Ni during sample preparation for XPS test.

$\text{Cu } 2p_{3/2}$ XPS spectra of the samples are shown in Fig. 5b. For $\text{NiO}_{0.5}\text{Cu}_{0.5}\text{CeO}_2$, two peaks and one satellite peak are observed at 930.0, 931.3, and 940–945 eV, respectively. The peak at 931.3 eV and the satellite peak are attributed to Cu^{2+} while the peak at 930.0 eV is associated with metallic Cu° and Cu^+ which have essentially identical binding energy [59]. Since the sample, however, is an oxide, the peak at 930.0 eV is solely for Cu^+ . As noted earlier, Cu^+ species which are able to form part of Cu-O-Ce structure can be generated and strongly stabilized by the strong interaction of CuO with CeO_2 [50–52]. For all the reduced samples, the intensity of the Cu^{2+} peaks at 931.3 eV and 940–945 eV decreases significantly, resulting from the reduction of Cu^{2+} to Cu° on the surface. Thus, Cu species in the reduced catalysts mainly exist in the form of metallic Cu and Cu-O-Ce solid solution. A small quantity of Cu^{2+} , however, still exists due to the surface oxidation during exposure of the samples to air.

Fig. 5c shows the Ce 3d XPS spectra of the samples. The spectra of Ce 3d can be split into a superposition of ten subpeaks at 880.8, 882.4, 885.0, 888.3, 898.2, 899.0, 901.1, 903.1, 907.1, and 916.6 eV. The four subpeaks at 880.8, 885.0, 899.0, and 903.1 eV are attributed to Ce^{3+} and the other six peaks are assigned to Ce^{4+} [60]. The ratio of integrated peak areas of Ce^{3+} to that of total Ce^{3+} and Ce^{4+} was calculated to estimate Ce^{3+} concentrations in the samples. The Ce^{3+} concentration of Cu/CeO_2 (21.8%) is relatively higher than for the Ni/CeO_2 (9.6%). As noted previously, owing to the similarity of ionic radius of Cu^+ (0.096 nm) and Ce^{4+} (0.094 nm), Cu can easily incorporate into the CeO_2 lattice as compared to Ni (0.072 nm), leading to more formation of the solid solution and the oxygen vacancy that essentially accompanies the formation of Ce^{3+} [46,50]. For the NiCu/CeO_2 samples, the Ce^{3+} concentration of $\text{Ni}_{0.75}\text{Cu}_{0.25}/\text{CeO}_2$, $\text{Ni}_{0.5}\text{Cu}_{0.5}/\text{CeO}_2$, and $\text{Ni}_{0.25}\text{Cu}_{0.75}/\text{CeO}_2$ is 28.5, 43.2, and 36.0%. The proportion of Ce^{3+} in the bimetallic catalysts is much higher as compared to the monometallic counterparts. It may be ascribed to the increased concentration of Cu^+ by the synergistic interaction between Ni, Cu, and CeO_2 . The highest Ce^{3+} concentration (43.2%) was found for $\text{Ni}_{0.5}\text{Cu}_{0.5}/\text{CeO}_2$ catalyst. Notably, the XPS results agree well with the XRD analysis that the CeO_2 lattice parameter of the NiCu/CeO_2 catalysts significantly increases due to the enhanced formation of the solid solution.

3.2.5. Raman measurements

The Raman spectra of the $\text{Ni}_{1-x}\text{Cu}_x/\text{CeO}_2$ catalysts ($x = 0, 0.25, 0.5, 0.75$, and 1) are shown in Fig. 6. A characteristic strong F_{2g} band at 463 cm^{-1} of cubic fluorite structured CeO_2 and a broad D band near 550 cm^{-1} were observed. The F_{2g} band is owing to a symmetrical stretching mode of oxygen atoms around each Ce^{4+} cation while the D band indicates the presence of oxygen vacancy (defect) in CeO_2 structure that may result from the formation of solid solution [61]. For the Ni/CeO_2 and Cu/CeO_2 , the intensity of the D band for the Cu/CeO_2 catalyst is stronger than that of Ni/CeO_2 , corresponding to higher concentration of the oxygen vacancy owing to the ability of Cu^+ to easily enter the CeO_2 lattice. In addition, for the NiCu/CeO_2 catalysts, the significant increase in the intensity of the D band is observed as compared to the monometallic counterparts. As noted above, it may be due to the synergistic interaction between Ni, Cu, and CeO_2 . The broadening and red-shift of the F_{2g} band for the NiCu/CeO_2 also resulted from the increased oxygen vacancies which can lead to the severe distortion of CeO_2 structure [62]. The Raman results indicate that the $\text{Ni}_{0.5}\text{Cu}_{0.5}/\text{CeO}_2$ catalyst has the highest concentration of oxygen vacancy, which is consistent with the XRD and XPS results.

3.2.6. H_2 -temperature programmed reduction (H_2 -TPR) analysis

The oxygen vacancy in the CeO_2 for CeO_2 supported metal oxides is known to diffuse to the surface oxygen of metal oxides and promote

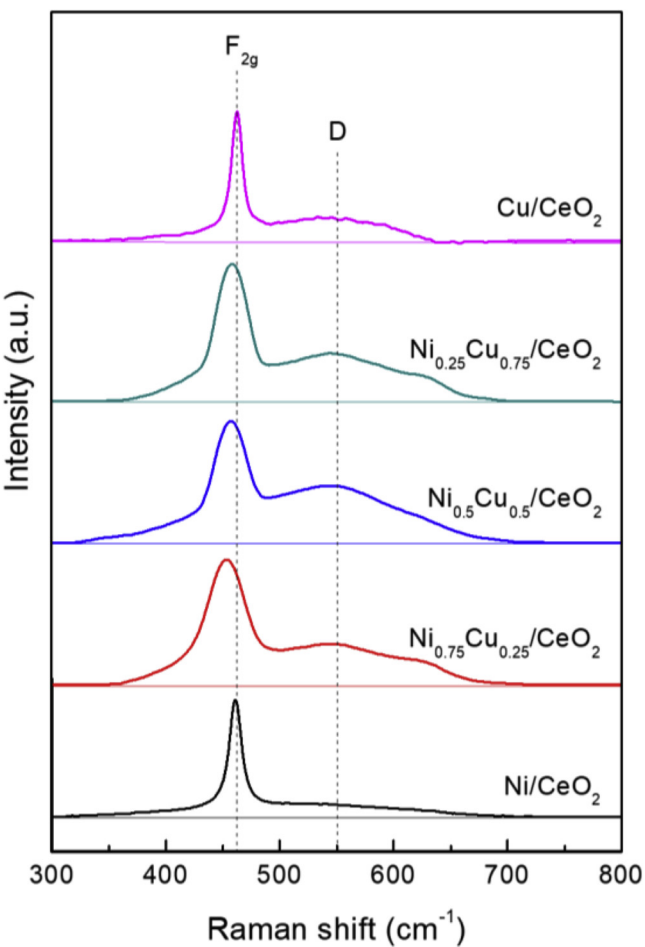


Fig. 6. Raman spectra of $\text{Ni}_{1-x}\text{Cu}_x/\text{CeO}_2$ ($x = 0, 0.25, 0.5, 0.75$, and 1) catalysts.

their reducibility under H_2 atmosphere by facilitating the dissociation of H_2 [63,64]. Accordingly, the synergistic formation of oxygen vacancies in CeO_2 by a strong interaction among Ni, Cu and CeO_2 was confirmed using H_2 -temperature-programmed reduction (H_2 -TPR) analysis. Fig. 7 shows the H_2 -TPR profiles of $\text{Ni}_{1-x}\text{Cu}_x/\text{CeO}_2$ ($x = 0, 0.25, 0.5, 0.75$, and 1) catalysts. For the Ni/CeO_2 , a broad hydrogen consumption peak (α) at 430°C was observed, which is ascribed to reduction of bulk NiO , while the Cu/CeO_2 showed a broad peak (β) at 300°C owing to reduction of bulk CuO [65]. For both Ni/CeO_2 and Cu/CeO_2 , a shoulder peak appears on the low temperature side of the α and β peaks. This shoulder is associated with the reduction of highly dispersed metal oxides (NiO or CuO) on CeO_2 . In the cases of NiCu/CeO_2 , α and β peaks shifted towards lower temperature as compared to that of Ni/CeO_2 and Cu/CeO_2 , suggesting that the reducibility of the NiCu/CeO_2 samples is substantially enhanced owing to the increased concentration of oxygen vacancies by a synergistic interaction among Ni, Cu and CeO_2 . As observed in the XRD measurements, the metal components of the NiCu/CeO_2 samples exist in NiCu alloy and Cu phases. Therefore, the NiCu alloying could also contribute to enhancing the reducibility of Ni phase (α peak). Ashok et al. reported that the Cu doped in Ni-Cu alloy catalysts leads to spillover hydrogen, which accelerates the nucleation of metallic Ni and enhances the reducibility of NiO at low temperature [66].

When the Cu content increases from 0.25 to 0.5, the α and β peaks shifted slightly further to lower temperature, while, with an increase of the Cu content from 0.5 to 0.75, the peaks shifted towards higher temperature. This feature is in accordance with the trend of concentration variation of oxygen vacancy observed from XRD, XPS, and

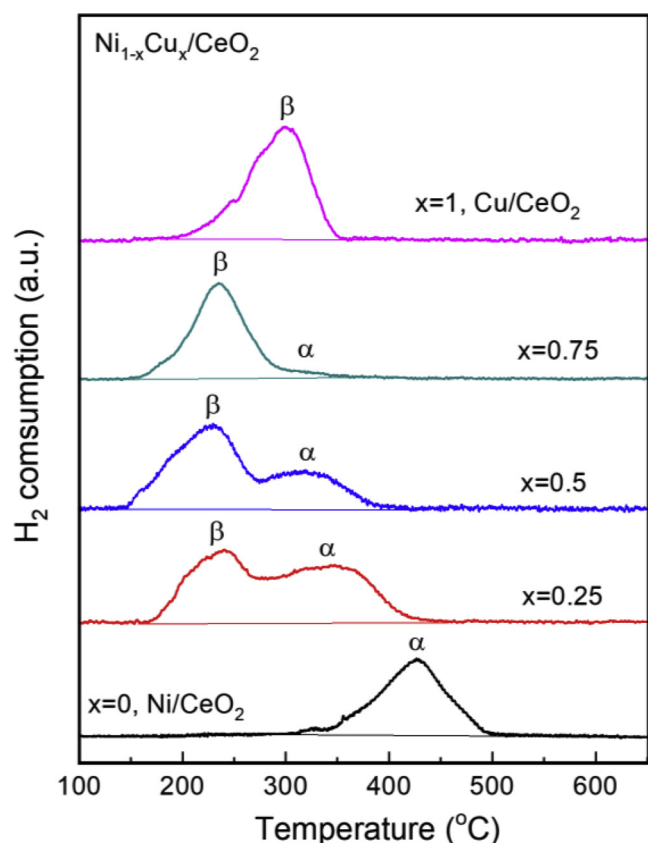


Fig. 7. H_2 -TPR profiles of $Ni_{1-x}Cu_x/CeO_2$ ($x = 0, 0.25, 0.5, 0.75$, and 1) catalysts.

Raman analysis. It is also seen that the intensity of the α peak becomes negligible for the $Ni_{0.25}Cu_{0.75}/CeO_2$, suggesting that most of Ni^{2+} ions incorporate into the CeO_2 structure and present as a form of Ni - O - Ce solid solutions, which is very stable structure and can be reduced at > 900 $^{\circ}C$, rather than bulk NiO particles. It is known that too much concentration of the solid solution with too little active Ni species in catalysts is unfavorable for hydrogen generation from hydrous hydrazine decomposition because the solid solution acts as a promoter but not an active site by itself [24,61].

The above characterization results indicate that the better catalytic performance of the $NiCu/CeO_2$ catalysts is related to the formation of more oxygen vacancies, which act as a promoter for the reaction, as well as $NiCu$ alloying and particle size of the active component. With increasing the Cu content from $x = 0$ to 0.5 , the concentration of oxygen vacancy in CeO_2 increases and thereby the catalytic activity increases with 100% H_2 selectivity. When the Cu content increases further from $x = 0.5$ to 0.75 , the activity and selectivity, however, decrease possibly due to a decreased amount of oxygen vacancy and too little active Ni atoms. It should be noted that the formation of a solid solution between metal ions and CeO_2 depends on the synthesis methods and SCS is reported to be an effective way to prepare a solid solution owing to the exothermic nature of combustion process [67,68]. Therefore, the formation of solid solutions in the $NiCu/CeO_2$ catalysts prepared by SCS may be ascribed to the synergistic interaction between Ni , Cu , and CeO_2 as well as the preparation method. All these possible reasons lead to the best catalytic performance of the $Ni_{0.5}Cu_{0.5}/CeO_2$ catalyst for hydrogen generation via hydrous hydrazine decomposition.

4. Conclusions

In this work, noble-metal-free $NiCu/CeO_2$ bimetallic catalysts with 13 wt% total metal loading were synthesized using a facile one-step SCS

method for hydrogen generation from hydrous hydrazine, which is a promising liquid-phase hydrogen carrier for fuel cell vehicles. The catalytic activity of the $NiCu/CeO_2$ for hydrogen generation was significantly enhanced as compared to their monometallic counterparts. The catalyst characterization revealed that $NiCu$ alloying, particle size of the active component, and concentration of the oxygen vacancy in CeO_2 lattice play an important role in the catalytic activity and selectivity. The alloying of Ni and Cu leads to modification of the electronic structure on the metal surface, which consequently improves the reactivity of the metals. The addition of Cu results in formation of more oxygen vacancy, which acts as a promoter for the reaction, by a strong synergistic interaction among Ni , Cu and CeO_2 . Besides, the SCS system for the $NiCu/CeO_2$ catalysts exhibits lower combustion temperature as compared to the system for monometallic counterparts, yielding smaller particle size which is beneficial for promoting the catalytic activity. The $Ni_{0.5}Cu_{0.5}/CeO_2$ catalyst possessing the smallest metal particle size and the highest amount of the oxygen vacancy showed 100% H_2 selectivity in the temperature range 30 – 70 $^{\circ}C$ and 3.2-fold higher TOF value of 1450.0 h^{-1} at 50 $^{\circ}C$ than that of the Ni/CeO_2 monometallic catalyst. This reactivity is also superior to that of most reported non-noble metal catalysts and is even comparable to several noble metal-based catalysts (see Table S2). Investigating support effects, the $Ni_{0.5}Cu_{0.5}/SiO_2$ shows much lower activity as compared to $Ni_{0.5}Cu_{0.5}/CeO_2$ despite the fact that they have similar metal particle size and degree of alloying. This suggests that the strong interaction between Ni , Cu , and CeO_2 , which generates a large amount of oxygen vacancy, may be the main reason for enhanced catalytic performance of $NiCu/CeO_2$.

This work demonstrates that SCS is an effective method to develop catalysts for hydrogen generation from hydrous hydrazine decomposition and the catalytic performance can be improved through a proper selection of secondary metal and catalyst preparation method. The efficient and cost-effective $Ni_{0.5}Cu_{0.5}/CeO_2$ catalyst may further encourage the practical application of hydrous hydrazine as a promising on-board hydrogen carrier for fuel cell vehicles. Finally, the synergistic effect found in this study may have significance in designing CeO_2 supported catalysts for other applications.

Acknowledgments

The authors gratefully thank the Davidson School of Chemical Engineering and the Slayer discretionary fund for support of this work.

Appendix A. Supplementary data

Supplementary material related to this article can be found, in the online version, at doi:<https://doi.org/10.1016/j.apcatb.2019.02.066>.

References

- [1] H.T. Hwang, A. Varma, Curr. Opin. Chem. Eng. 5 (2014) 42–48.
- [2] T. He, P. Pachfule, H. Wu, Q. Xu, P. Chen, Nat. Rev. Mater. 1 (2016) 16059.
- [3] P. Preuster, C. Papp, P. Wasserscheid, Accounts Chem. Res. 50 (2017) 74–85.
- [4] Q.-L. Zhu, Q. Xu, Energy Environ. Sci. 8 (2015) 478–512.
- [5] S.K. Singh, Q. Xu, Catal. Sci. Technol. 3 (2013) 1889–1900.
- [6] B.C.H. Steele, A. Heinzel, Nature 414 (2001) 345–352.
- [7] B.T. Zhao, J. Song, R. Ran, Z.P. Shao, Int. J. Hydrogen Energy 37 (2012) 1133–1139.
- [8] X. Cheng, Z. Shi, N. Glass, L. Zhang, J.J. Zhang, D.T. Song, Z.S. Liu, H.J. Wang, J. Shen, J. Power Sources 165 (2007) 739–756.
- [9] R. Halseid, P.J.S. Vie, R. Tunold, J. Power Sources 154 (2006) 343–350.
- [10] S.K. Singh, X.B. Zhang, Q. Xu, J. Am. Chem. Soc. 131 (2009) 9894–9895.
- [11] S.K. Singh, Q. Xu, J. Am. Chem. Soc. 131 (2009) 18032–18033.
- [12] S.K. Singh, Y. Iizuka, Q. Xu, Int. J. Hydrogen Energy 36 (2011) 11794–11801.
- [13] D. Bhattacharjee, S. Dasgupta, J. Mater. Chem. A 3 (2015) 24371–24378.
- [14] J. Wang, W. Li, Y.R. Wen, L. Gu, Y. Zhang, Adv. Energy Mater. 5 (2015) 1401879.
- [15] P.P. Zhao, N. Cao, J. Su, W. Luo, G.Z. Cheng, ACS Sustain. Chem. Eng. 3 (2015) 1086–1093.
- [16] X.Q. Du, C. Liu, C. Du, P. Cai, G.Z. Cheng, W. Luo, Nano Res. 10 (2017) 2856–2865.
- [17] S.K. Singh, A.K. Singh, K. Aranishi, Q. Xu, J. Am. Chem. Soc. 133 (2011)

19638–19641.

[18] K.V. Manukyan, A. Cross, S. Rouvimov, J. Miller, A.S. Mukasyan, E.E. Wolf, *Appl. Catal. A* 476 (2014) 47–53.

[19] H.L. Wang, J.M. Yan, S.J. Li, X.W. Zhang, Q. Jiang, *J. Mater. Chem. A* 3 (2015) 121–124.

[20] L. He, Y.Q. Huang, A.Q. Wang, X.D. Wang, X.W. Chen, J.J. Delgado, T. Zhang, *Angew. Chem. Int. Ed.* 51 (2012) 6191–6194.

[21] W. Gao, C.M. Li, H. Chen, M. Wu, S. He, M. Wei, D.G. Evans, X. Duan, *Green Chem.* 16 (2014) 1560–1568.

[22] D.D. Wu, M. Wen, X.J. Lin, Q.S. Wu, C. Gu, H.X. Chen, *J. Mater. Chem. A* 4 (2016) 6595–6602.

[23] D.D. Wu, M. Wen, C. Gu, Q.S. Wu, *ACS Appl. Mater. Inter.* 9 (2017) 16103–16108.

[24] L. He, B.L. Liang, L. Li, X.F. Yang, Y.Q. Huang, A.Q. Wang, X.D. Wang, T. Zhang, *ACS Catal.* 5 (2015) 1623–1628.

[25] Y.J. Zhong, H.B. Dai, M. Zhu, P. Wang, *Int. J. Hydrogen Energy* 41 (2016) 11042–11049.

[26] B.Q. Xia, T. Liu, W. Luo, G.Z. Cheng, *J. Mater. Chem. A* 4 (2016) 5616–5622.

[27] A. Varma, A.S. Mukasyan, A.S. Rogachev, K.V. Manukyan, *Chem. Rev.* 116 (2016) 14493–14586.

[28] W. Kang, A. Varma, *Appl. Catal. B* 220 (2018) 409–416.

[29] L.C. Chen, S.D. Lin, *Appl. Catal. B* 106 (2011) 639–649.

[30] E.T. Saw, U. Oemar, X.R. Tan, Y. Du, A. Borgna, K. Hidajat, S. Kawi, *J. Catal.* 314 (2014) 32–46.

[31] G. Ertl, H. Knözinger, J. Weitkamp, *Handbook of Heterogeneous Catalysis*, VCH, Weinheim, 1997.

[32] H.A. Yen, Y. Seo, S. Kaliaguine, F. Kleitz, *ACS Catal.* 5 (2015) 5505–5511.

[33] K. Aranishi, A.K. Singh, Q. Xu, *ChemCatChem* 5 (2013) 2248–2252.

[34] L. He, Y.Q. Huang, A.Q. Wang, Y. Liu, X.Y. Liu, X.W. Chen, J.J. Delgado, X.D. Wang, T. Zhang, *J. Catal.* 298 (2013) 1–9.

[35] D.G. Tong, D.M. Tang, W. Chu, G.F. Gu, P. Wu, *J. Mater. Chem. A* 1 (2013) 6425–6432.

[36] H. Dai, Y.P. Qiu, H.B. Dai, P. Wang, *Int. J. Hydrogen Energy* 42 (2017) 16355–16361.

[37] M. Thommes, K. Kaneko, A.V. Neimark, J.P. Olivier, F. Rodriguez-Reinoso, J. Rouquerol, K.S.W. Sing, *Pure Appl. Chem.* 87 (2015) 1051–1069.

[38] F. Studt, F. Abild-Pedersen, Q. Wu, A.D. Jensen, B. Temel, J.-D. Grunwaldt, J.K. Nørskov, *J. Catal.* 293 (2012) 51–60.

[39] Y. Shen, Y. Zhou, D. Wang, X. Wu, J. Li, J. Xi, *Adv. Energy Mater.* 8 (2018) 1701759.

[40] K. Ray, G. Deo, *Appl. Catal. B* 218 (2017) 525–537.

[41] Q.F. Zhang, X.P. Wu, Y.K. Li, R.J. Chai, G.F. Zhao, C.Z. Wang, X.Q. Gong, Y. Liu, Y. Lu, *ACS Catal.* 6 (2016) 6236–6245.

[42] S.H. Ahn, H.Y. Park, I. Choi, S.J. Yoo, S.J. Hwang, H.J. Kim, E. Cho, C.W. Yoon, H. Park, H. Son, J.M. Hernandez, S.W. Nam, T.H. Lim, S.K. Kim, J.H. Jang, *Int. J. Hydrogen Energy* 38 (2013) 13493–13501.

[43] B.D. Cullity, S.R. Stock, *Elements of X-Ray Diffraction*, 3rd ed., Prentice Hall, Upper Saddle River, NJ, 2001.

[44] S.M. Sun, X.L. Zhao, H. Lu, Z.D. Zhang, J.J. Wei, Y.Z. Yang, *CrystEngComm* 15 (2013) 1370–1376.

[45] J.F. Chen, Y.Y. Zhan, J.J. Zhu, C.Q. Chen, X.Y. Lin, Q. Zheng, *Appl. Catal. A Gen.* 377 (2010) 121–127.

[46] C.P. Poole, V.G. Bar'akhtar, *Encyclopedic Dictionary of Condensed Matter Physics*, 1st ed., Elsevier, Amsterdam ; Boston, 2004.

[47] B. Yan, X. Yang, S. Yao, J. Wan, M. Myint, E. Gomez, Z. Xie, S. Kattel, W. Xu, J.G. Chen, *ACS Catal.* 6 (2016) 7283–7292.

[48] F. Wang, S. He, H. Chen, B. Wang, L.R. Zheng, M. Wei, D.G. Evans, X. Duan, *J. Am. Chem. Soc.* 138 (2016) 6298–6305.

[49] S.D. Senanayake, P.J. Ramirez, I. Waluyo, S. Kundu, K. Mudiyanselage, Z.Y. Liu, Z. Liu, S. Axnanda, D.J. Stacchiola, J. Evans, J.A. Rodriguez, *J. Phys. Chem. C* 120 (2016) 1778–1784.

[50] G.X. Chen, Q.L. Li, Y.C. Wei, W.P. Fang, Y.Q. Yang, *Chin. J. Catal.* 34 (2013) 322–329.

[51] W. Liu, M. Flytzanistefanopoulos, *J. Catal.* 153 (1995) 304–316.

[52] M. Turco, C. Cammarano, G. Bagnasco, E. Moretti, L. Storaro, A. Talon, M. Lenarda, *Appl. Catal. B* 91 (2009) 101–107.

[53] S. Deshpande, S. Patil, S.V.N.T. Kuchibhatla, S. Seal, *Appl. Phys. Lett.* 87 (2005) 133113.

[54] R.K. Hailstone, A.G. DiFrancesco, J.G. Leong, T.D. Allston, K.J. Reed, *J. Phys. Chem. C* 113 (2009) 15155–15159.

[55] A.R. Naghash, T.H. Etsell, S. Xu, *Chem. Mater.* 18 (2006) 2480–2488.

[56] W. Shan, M. Luo, P. Ying, W. Shen, C. Li, *Appl. Catal. A* 246 (2003) 1–9.

[57] H. Wei, K. Xie, J. Zhang, Y. Zhang, Y. Wang, Y. Qin, J. Cui, J. Yan, Y. Wu, *Sci. Rep.* 4 (2014) 5156.

[58] P.F. Barbieri, A. de Siervo, M.F. Carazzolle, R. Landers, G.G. Kleiman, *J. Electron Spectros. Relat. Phenomena* 135 (2004) 113–118.

[59] N. Pauly, S. Tougaard, F. Yubero, *Surf. Sci.* 620 (2014) 17–22.

[60] G.B. Della Mea, L.P. Matte, A.S. Thill, F.O. Lobato, E.V. Benvenutti, L.T. Arenas, A. Jurgensen, R. Hergenroder, F. Poletto, F. Bernardi, *Appl. Surf. Sci.* 422 (2017) 1102–1112.

[61] W. Kang, D.O. Ozgur, A. Varma, *ACS Appl. Nano Mater.* (2018).

[62] Z.L. Wu, M.J. Li, J. Howe, H.M. Meyer, S.H. Overbury, *Langmuir* 26 (2010) 16595–16606.

[63] S.H. Kim, W.D. Lee, H.I. Lee, *Korean J. Chem. Eng.* 30 (2013) 860–863.

[64] S.Q. Chen, L.P. Li, W.B. Hu, X.S. Huang, Q. Li, Y.S. Xu, Y. Zuo, G.S. Li, *ACS Appl. Mater. Inter.* 7 (2015) 22999–23007.

[65] T. Liang, Y. Wang, M. Chen, Z. Yang, S. Liu, Z. Zhou, X. Li, *Int. J. Hydrogen Energy* 42 (2017) 28233–28246.

[66] J. Ashok, Y. Kathiraser, M.L. Ang, S. Kawi, *Catal. Sci. Technol.* 5 (2015) 4398–4409.

[67] B. Murugan, A.V. Ramaswamy, D. Srinivas, C.S. Gopinath, V. Ramaswamy, *Chem. Mater.* 17 (2005) 3983–3993.

[68] M.S. Hegde, P. Beraba, *Catal. Today* 253 (2015) 40–50.